

Scattering and Imaging of Nonlinearly Loaded Antenna Structures in Half-Space and Complex-Room Environments

by DaHan Liao and Traian Dogaru

ARL-TR-7116

September 2014

NOTICES

Disclaimers

The findings in this report are not to be construed as an official Department of the Army position unless so designated by other authorized documents.

Citation of manufacturer's or trade names does not constitute an official endorsement or approval of the use thereof.

Destroy this report when it is no longer needed. Do not return it to the originator.

Army Research Laboratory

Adelphi, MD 20783-1138

ARL-TR-7116

September 2014

Scattering and Imaging of Nonlinearly Loaded Antenna Structures in Half-Space and Complex-Room Environments

DaHan Liao and Traian Dogaru
Sensors and Electron Devices Directorate, ARL

REPORT DOCUMENTATION PAGE				Form Approved OMB No. 0704-0188	
<p>Public reporting burden for this collection of information is estimated to average 1 hour per response, including the time for reviewing instructions, searching existing data sources, gathering and maintaining the data needed, and completing and reviewing the collection information. Send comments regarding this burden estimate or any other aspect of this collection of information, including suggestions for reducing the burden, to Department of Defense, Washington Headquarters Services, Directorate for Information Operations and Reports (0704-0188), 1215 Jefferson Davis Highway, Suite 1204, Arlington, VA 22202-4302. Respondents should be aware that notwithstanding any other provision of law, no person shall be subject to any penalty for failing to comply with a collection of information if it does not display a currently valid OMB control number.</p> <p>PLEASE DO NOT RETURN YOUR FORM TO THE ABOVE ADDRESS.</p>					
1. REPORT DATE (DD-MM-YYYY) September 2014		2. REPORT TYPE		3. DATES COVERED (From - To) 2013–2014	
4. TITLE AND SUBTITLE Scattering and Imaging of Nonlinearly Loaded Antenna Structures in Half-Space and Complex-Room Environments				5a. CONTRACT NUMBER	
				5b. GRANT NUMBER	
				5c. PROGRAM ELEMENT NUMBER	
6. AUTHOR(S) DaHan Liao and Traian Dogaru				5d. PROJECT NUMBER	
				5e. TASK NUMBER	
				5f. WORK UNIT NUMBER	
7. PERFORMING ORGANIZATION NAME(S) AND ADDRESS(ES) U.S. Army Research Laboratory ATTN: RDRL-SER-U 2800 Powder Mill Road Adelphi, MD 20783-1138				8. PERFORMING ORGANIZATION REPORT NUMBER ARL-TR-7116	
9. SPONSORING/MONITORING AGENCY NAME(S) AND ADDRESS(ES)				10. SPONSOR/MONITOR'S ACRONYM(S)	
				11. SPONSOR/MONITOR'S REPORT NUMBER(S)	
12. DISTRIBUTION/AVAILABILITY STATEMENT Approved for public release; distribution unlimited.					
13. SUPPLEMENTARY NOTES					
14. ABSTRACT <p>The electromagnetic scattering responses of nonlinearly loaded antenna structures excited by single-tone or multi-tone incident fields are considered in the frequency domain by employing a combination of the method-of-moments and a harmonic balance technique. Subsequently, standoff detection and localization of the scatterers in the presence of a half-space or within a complex room is demonstrated with a subspace imaging procedure by exploiting the steady-state, multistatic harmonic scattering responses collected over an aspect-limited aperture. For the half-space problem, the attenuation rates of the harmonic scattered fields as a function of sensing range are investigated; the Green's function vector in the imaging functional is derived efficiently with the application of second-order-accurate asymptotic propagation techniques; and near-field imaging performance for single and multiple targets is also examined in the presence of noise and linear clutter. For the sensing-through-the-wall problem, the effectiveness of the imaging technique is analyzed with the assumption that the complex-room environment Green's function is not known <i>a priori</i>. This study is intended to provide an analysis and simulation framework needed to facilitate the development of a complementary nonlinear detection capability for an existing near-ground, forward-looking linear imaging radar system.</p>					
15. SUBJECT TERMS Computational Electromagnetics, Radar					
16. SECURITY CLASSIFICATION OF:			17. LIMITATION OF ABSTRACT UU	18. NUMBER OF PAGES 36	19a. NAME OF RESPONSIBLE PERSON DaHan Liao
a. REPORT Unclassified	b. ABSTRACT Unclassified	c. THIS PAGE Unclassified			19b. TELEPHONE NUMBER (Include area code) 301-394-1741

Contents

List of Figures	iv
1. Introduction	1
2. Analysis and Simulation Framework	2
2.1 Linear and Nonlinear Scattering Characterization	3
2.2 Subspace-Based Image Formation	4
3. Numerical Experiment Results	6
3.1 Sensing in Half-Space Environment	7
3.2 Sensing in Complex-Room Environment.....	15
4. Conclusions	19
5. References	20
Appendix A. Variable Definitions for Section 2.1	23
Appendix B. Asymptotic Green's Function Definitions for Half-Space	27
Distribution List	30

List of Figures

Fig. 1 Standoff sensing of nonlinearly loaded antenna structure in a half-space environment in the presence of clutter	3
Fig. 2 Monostatic scattered electric field strength for center array element: a) Single-tone excitation at 300 MHz; three diode-loaded targets and b) Two-tone excitation at 300 MHz and 305 MHz; two varactor-loaded targets	8
Fig. 3 Normalized singular value spectrum: a) Three diode-loaded targets and b) Two varactor-loaded targets.....	9
Fig. 4 Three diode-loaded vertical dipole antennas; single-tone excitation ($ \Omega^\alpha = Q = 1$) at 300 MHz (transmitted power: 4 W). $ \Omega^\beta = P = 10$. Imaging formation frequencies: 600 MHz, 900 MHz, 1500 MHz, 2100 MHz. a) SNR = ∞ (no noise); b) SNR = 30 dB; c) SNR = 20 dB; and d) SNR = 10 dB. Circled numbers denote nonlinear targets. The image intensity is displayed in dB scale.	10
Fig. 5 Two varactor-loaded vertical dipole antennas; double-tone excitation ($ \Omega^\alpha = Q = 2$) at 300 MHz and 305 MHz (transmitted power: 1.7 W). $ \Omega^\beta = P = 12$. Imaging formation frequencies: 600 MHz, 605 MHz, 610 MHz. a) SNR = ∞ (no noise); b) SNR = 30 dB; c) SNR = 20 dB; and d) SNR = 10 dB.....	12
Fig. 6 Same scenarios as those in Figs. 4 and 5, except scatterer 2 is a linear clutter object. SNR = 20 dB.....	13
Fig. 7 a) Two diode-loaded horizontal dipole antennas and b) One diode-loaded horizontal dipole antenna (scatterer 1) and one linear clutter object (scatterer 2). Single-tone excitation ($ \Omega^\alpha = Q = 1$) at 300 MHz (transmitted power: 4 W). $ \Omega^\beta = P = 10$. Imaging formation frequencies: 300 MHz, 600 MHz, and SNR = 20 dB.	14
Fig. 8 Two diode-loaded horizontal dipole antennas (scatterers 1 and 4) in a clutter field: a) On-surface and b) Buried. Scatterer 2 is a vertical dipole; scatterer 3 is a horizontal dipole; scatterers 5 and 6 are metallic cylinders. Single-tone excitation ($ \Omega^\alpha = Q = 1$) at 300 MHz (transmitted power: 4 W). $ \Omega^\beta = P = 10$. Imaging formation frequencies: 300 MHz, 1200 MHz, and SNR = 20 dB.....	15
Fig. 9 a) Diode-loaded dipole antenna in a complex-room environment— position 1 and b) Imaging result with single-tone excitation ($ \Omega^\alpha = Q = 1$) at 300 MHz (transmitted power: 4 W). $ \Omega^\beta = P = 10$. Imaging formation frequency: 600 MHz, SNR = 20 dB.	16
Fig. 10 a) Diode-loaded dipole antenna in a complex-room environment— position 2 and b) Imaging result with single-tone excitation ($ \Omega^\alpha = Q = 1$) at 300 MHz (transmitted power: 4 W). $ \Omega^\beta = P = 10$. Imaging formation frequency: 600 MHz, SNR = 20 dB.	17
Fig. 11 a) Diode-loaded dipole antenna in a complex-room environment— position 3 and b) Imaging result with single-tone excitation ($ \Omega^\alpha = Q = 1$) at 300 MHz (transmitted power: 4 W). $ \Omega^\beta = P = 10$. Imaging formation frequency: 600 MHz, SNR = 20 dB.	18

1. Introduction

The characterization of the scattering responses of nonlinear circuit-element-loaded scatterers is an important problem in both electromagnetic interference and remote sensing applications. As pertinent to communication systems design, it is well-known that nonlinearly modulated scattering phenomena constitute a factor in understanding how inter-coupling effects among different radios influence transceiver performance and signal fidelity. Fundamentally, from the sensing perspective, a nonlinearly loaded target—when properly excited—could potentially re-radiate unique features, enabling it to be differentiated from an ordinary scatterer. For example, the antenna, filter, and amplifier block at the RF front-end of the receiver of an electronic device can modulate a probing signal, facilitating opportunities for signature classification and detection—in particular, the presence of nonlinear components can lead to harmonic signal generation within the electronic system and subsequent unintended re-emissions through the antenna port; these re-emissions, in turn, can be exploited to aid the extraction of the target embedded in linear clutter. From the radar implementation perspective, the tantalizing prospect of "clutter-free" detection has been previously discussed in literature in conjunction with the introduction of the harmonic radar.^{1,2} Within the above prescribed context, the electromagnetic characterization of nonlinearly loaded antennas in itself is seen to be an important sub-problem that deserves further in-depth consideration. Accordingly, in this study, both the harmonic scattering and imaging responses of nonlinearly loaded antennas located in the presence of a half-space environment or within a complex-room environment are investigated—with specific relevance to active RF sensing, detection, and localization.

The electromagnetic behavior of nonlinearly loaded radiators has been a subject of interest in many studies. A variety of direct time-domain integral equation methods have been proposed for analyzing nonlinearly loaded wire antennas.^{3–6} Volterra series analysis is adapted in⁷ for modeling the nonlinear antenna system after transforming the electromagnetic problem into a nonlinear network using the method-of-moments. The focus of more recent studies has been on frequency domain methods: in,⁸ a harmonic balance technique is introduced for simulating scattering from wire scatterers with nonlinear loads; in,^{9–12} several techniques are proposed for treating either the single dipole or an array of dipoles, including the reflection method, the application of neural networks, and the harmonic balance method in combination with the inexact Newton approach or the particle swarm algorithm. All of the aforementioned studies assume the antenna is in a free space environment; the inclusion of lossy ground effects in calculating the nonlinear response, however, is considered in^{13–16}—where the antenna is placed above the ground surface. It also should be mentioned that the scopes of these studies do not fully encompass the remote sensing problem—that is, the discussions therein do not consider the localization of the loaded radiator by exploiting the nonlinear scattering response.

Spatial and spectral array signal processing techniques can be used for interpreting the information embedded in the scattering returns in order to localize the nonlinearly loaded antenna target. For example, in active sensing—analogue to the case of the ultra-wideband linear radar system—after sweeping over a band of interrogation frequencies and subsequently capturing the scattering responses at the harmonic frequencies, an extension of the conventional time-reversal method^{17–19} may be employed for target imaging purposes. The application of such a sensing approach would enable the target to be isolated from surrounding linear clutter; however, a rigorous study in this area has not been carried out in existing works. A direction-of-arrival estimation technique—or its many variants, as applied to the harmonic returns—can also be used to resolve the angular position of the nonlinear source; furthermore, direction-of-arrival and time-of-arrival processing can be combined to obtain the absolute position of the target. A survey of the literature shows that in the harmonic radar community, several approaches are currently exploited for target tracking: for instance, in,²⁰ a harmonic radar direction finder is discussed; and in,²¹ a modified frequency modulated continuous wave radar is proposed for target range determination.

In this work, an investigation is performed to explore the feasibility and the mechanisms of using a subspace-based method for imaging a scene consisting of nonlinearly loaded antenna targets and linear clutter. The focus here is primarily on the half-space problem, as the study is intended to facilitate the development of a complementary nonlinear detection capability for an existing near-ground, forward-looking linear imaging radar system introduced in.²² As such, the theoretical formalism is first established purely in terms of the half-space detection problem before the complex-room sensing problem is considered as a special case. The overall work is put forth as follows: in Section 2, the analysis and simulation framework is delineated—first the formalisms of the solver for analyzing the linear and nonlinear multistatic scattered fields from nonlinearly loaded antennas are outlined, then the subspace imaging algorithm for processing the harmonic re-radiation is presented; in Section 3, the electromagnetic scattering and propagation solver and the harmonic imaging technique are applied to study the detection and localization of nonlinear targets in half-space and complex-room environments; and in Section 4, a summary of the investigation is given.

2. Analysis and Simulation Framework

As a starting point, standoff sensing scenarios akin to the one described in²³ are considered: a stationary N -element transmitter array is located above a perfectly flat, lossy ground; the scene is sparsely populated with scatterers, among which are the targets of interest (i.e., one or more nonlinearly loaded metallic antenna elements) positioned either above or below the ground surface (Fig. 1). The transmitter array is composed of infinitesimal dipoles, emitting either single-tone or multi-tone time-harmonic fields. The steady-state, multistatic scattered signals—at

the harmonic frequencies of the excitation frequencies—from the scene are captured at observation points co-located with the transmitters.

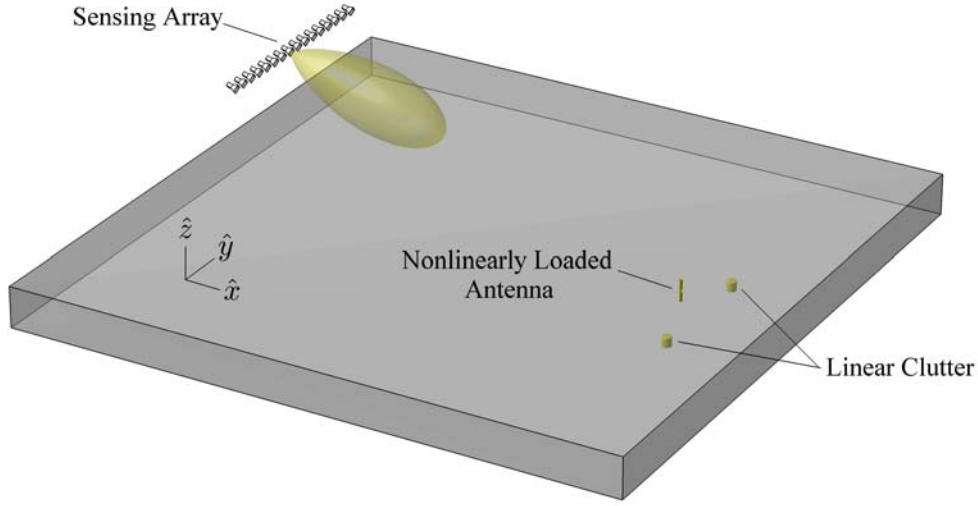


Fig. 1 Standoff sensing of nonlinearly loaded antenna structure in a half-space environment in the presence of clutter

2.1 Linear and Nonlinear Scattering Characterization

The incident fields at each antenna structure are calculated with the dyadic half-space (one-layer-medium) Green's function.²⁴ The responses, or induced currents, on the structure are deduced by exploiting a hybrid method-of-moments and equivalent circuit approach; the antenna input admittance Y_{ant} and Norton equivalent short-circuit current I_{sc} are first characterized at the relevant frequency points using the half-space mixed-potential integral equation solver,²⁵ and then—in the circuit domain—a harmonic balance technique⁸ is employed for obtaining the terminal voltage response V_{ant} of the antenna connected to the nonlinear load. In essence, after dividing the loaded antenna circuit into linear and nonlinear sections at the antenna terminal reference plane and applying the standard nodal current law, the following nonlinear matrix system can be established to solve for the terminal voltage response:

$$\bar{\bar{T}}_{f \leftarrow t} g\left(\bar{\bar{T}}_{t \leftarrow f} \mathbf{V}_{ant}\right) + \bar{\bar{Y}}_{ant} \mathbf{V}_{ant} - \mathbf{I}_{sc} + \bar{\bar{H}}\left(\frac{1}{R_b} \mathbf{V}_{ant} - \mathbf{c}\right) = 0, \quad (1)$$

which contingents on the suppositions

$$\mathbf{V}_{ant}(t) = V_{ant,DC} + \sum_{p=1}^P V_{ant,2p-1} \cos(\omega_p^\beta t) + V_{ant,2p} \sin(\omega_p^\beta t), \quad (2)$$

$$\mathbf{I}_{sc}(t) = \sum_{q=1}^Q I_{sc,2q-1} \cos(\omega_q^\alpha t) + I_{sc,2q} \sin(\omega_q^\alpha t); \quad (3)$$

P is the number of frequencies ($\omega_p^\beta \in \Omega^\beta$, or $f_p^\beta \in F^\beta$) employed in the harmonic balance technique; Q is the number of excitation tones ($\omega_q^\alpha \in \Omega^\alpha$, or $f_q^\alpha \in F^\alpha$, and $\Omega^\alpha \subset \Omega^\beta$, $F^\alpha \subset F^\beta$); \mathbf{V}_{ant} and \mathbf{I}_{sc} are defined using the coefficients of Equations 2 and 3; and $\bar{\bar{\mathbf{Y}}}_{ant}$ is the antenna admittance matrix covering the P frequencies of interest. The $i-v$ characteristic of the nonlinear load is $i(t) = g(v(t))$; transformations between the time and frequency domains are obtained with the matrices $\bar{\bar{\mathbf{T}}}_{f \leftarrow t}$ and $\bar{\bar{\mathbf{T}}}_{t \leftarrow f}$. Also note that the nonlinear load is biased with DC voltage V_b and resistor R_b (the bias inductor is ignored in the AC analysis); thus, in compact form, \mathbf{c} is a constant vector with all elements equal to V_b/R_b and $\bar{\bar{\mathbf{H}}}$ is non-zero only for the first element: $H_{11} = 1$. The solution to (1) is computed with the Newton-Raphson method, after deriving the Jacobian of the matrix system and properly defining $\bar{\bar{\mathbf{T}}}_{f \leftarrow t}$, $\bar{\bar{\mathbf{T}}}_{t \leftarrow f}$, and the time domain sampling rate and interval. (Additional definitions for variables related to Equation 1 are in Appendix A.) Subsequently, having deduced \mathbf{V}_{ant} , the induced currents on the antenna structure at each frequency are found with the aforementioned method-of-moments solver, and the scattered fields are propagated to the observation points using the same method as for calculating the incident excitation fields. In computing the scattered signal at the illumination frequencies ($\omega_p^\beta \in \Omega^\alpha$), the short-circuited antenna scattering pattern is added to the antenna re-radiation component to obtain the total scattering response.

Note that for the calculation of the dyadic half-space Green's function within the method-of-moments solver, exact Sommerfeld integrals are used. For the scattering and propagation routine, however, in order to increase the computational efficiency, second-order-accurate asymptotic approximations to these Sommerfeld integrals are employed instead:^{26,27} these asymptotic forms (Appendix B) are derived by applying the method of steepest descents to the integral expressions and provide the necessary accuracy to capture wave interactions at the near-ground region, including Norton surface wave effects²⁶—which can be of importance for near-grazing half-space propagation scenarios, depending on the physical parameters of the problem and the locations of the transceiver array and targets with respect to the ground interface.

2.2 Subspace-Based Image Formation

After the determination of the linear and nonlinear scattered signal, a subspace-based imaging technique similar to the time-reversal multiple signal classification method^{28–33} that has been developed for linear radar sensing is adapted for target localization. The mechanisms and formulations of the algorithm implemented herein are established as follows. Considering the case of M point-like targets at positions \mathbf{r}_m^β ($m \in \{1, 2, \dots, M\}$), and denoting the current on the n -th ($n \in \{1, 2, \dots, N\}$) transmitter—at frequency ω_q^α —as

$$\mathbf{J}_n(\mathbf{r}, \omega_q^\alpha) = I_{on}(\omega_q^\alpha) \left(\ell_{xn}(\omega_q^\alpha) \hat{\mathbf{x}} + \ell_{yn}(\omega_q^\alpha) \hat{\mathbf{y}} + \ell_{zn}(\omega_q^\alpha) \hat{\mathbf{z}} \right) \delta(\mathbf{r} - \mathbf{r}_n^\alpha), \quad (4)$$

the incident signal is

$$\mathbf{E}_i(\omega_q^\alpha) \in \mathbb{C}^{3M \times 1} = \bar{\bar{\mathbf{G}}}(\mathbf{r}^\beta, \mathbf{r}^\alpha, \omega_q^\alpha) \mathbf{I}(\omega_q^\alpha), \quad (5)$$

where $\mathbf{I}(\omega_q^\alpha) \in \mathbb{C}^{3N \times 1}$ contains the components of $\mathbf{J}_n(\mathbf{r}, \omega_q^\alpha)$ (for all N elements), $\mathbf{E}_i(\omega_q^\alpha)$

contains the excitation electric field evaluated at all M target points, and

$$\bar{\bar{\mathbf{G}}}(\mathbf{r}^\beta, \mathbf{r}^\alpha, \omega_q^\alpha) \in \mathbb{C}^{3M \times 3N} = \begin{bmatrix} \bar{\bar{\mathbf{G}}}_{\xi\eta}(\mathbf{r}_1^\beta, \mathbf{r}_1^\alpha, \omega_q^\alpha) & \bar{\bar{\mathbf{G}}}_{\xi\eta}(\mathbf{r}_1^\beta, \mathbf{r}_2^\alpha, \omega_q^\alpha) & \dots & \bar{\bar{\mathbf{G}}}_{\xi\eta}(\mathbf{r}_1^\beta, \mathbf{r}_N^\alpha, \omega_q^\alpha) \\ \bar{\bar{\mathbf{G}}}_{\xi\eta}(\mathbf{r}_2^\beta, \mathbf{r}_1^\alpha, \omega_q^\alpha) & \bar{\bar{\mathbf{G}}}_{\xi\eta}(\mathbf{r}_2^\beta, \mathbf{r}_2^\alpha, \omega_q^\alpha) & \dots & \bar{\bar{\mathbf{G}}}_{\xi\eta}(\mathbf{r}_2^\beta, \mathbf{r}_N^\alpha, \omega_q^\alpha) \\ \vdots & \vdots & \ddots & \vdots \\ \bar{\bar{\mathbf{G}}}_{\xi\eta}(\mathbf{r}_M^\beta, \mathbf{r}_1^\alpha, \omega_q^\alpha) & \bar{\bar{\mathbf{G}}}_{\xi\eta}(\mathbf{r}_M^\beta, \mathbf{r}_2^\alpha, \omega_q^\alpha) & \dots & \bar{\bar{\mathbf{G}}}_{\xi\eta}(\mathbf{r}_M^\beta, \mathbf{r}_N^\alpha, \omega_q^\alpha) \end{bmatrix}, \quad (6)$$

in which $\bar{\bar{\mathbf{G}}}_{\xi\eta}(\mathbf{r}_m^\beta, \mathbf{r}_n^\alpha, \omega_q^\alpha)$ is the dyadic half-space Green's function. Upon noting the reciprocity relation $\bar{\bar{\mathbf{G}}}_{\xi\eta}(\mathbf{r}_m^\beta, \mathbf{r}_n^\alpha, \omega_p^\beta) = \bar{\bar{\mathbf{G}}}_{\xi\eta}(\mathbf{r}_n^\alpha, \mathbf{r}_m^\beta, \omega_p^\beta)^T$, the scattered field at frequency ω_p^β at all N receiver positions can then be cast as

$$\mathbf{E}_s(\omega_p^\beta) \in \mathbb{C}^{3N \times 1} = \bar{\bar{\mathbf{G}}}(\mathbf{r}^\beta, \mathbf{r}^\alpha, \omega_p^\beta)^T \cdot \mathcal{L}(\mathbf{E}_i(\Omega^\alpha), \omega_p^\beta), \quad (7)$$

with $\mathcal{L}(\cdot)$ as the operator transforming excitation fields into radiation currents at \mathbf{r}_m^β . It is seen from Equation 7 that the scattered signal is a subspace spanned by the columns of $\bar{\bar{\mathbf{G}}}(\mathbf{r}^\beta, \mathbf{r}^\alpha, \omega_p^\beta)^T$ (that is, the Green's function vectors), and the scatterer positions are encoded within this representation. Transmitting the $3N$ dipole element components sequentially, a multistatic scattered field matrix $\bar{\bar{\mathbf{K}}}(\omega_p^\beta) \in \mathbb{C}^{3N \times 3N}$ can be obtained as

$$\bar{\bar{\mathbf{K}}}(\omega_p^\beta) = \begin{bmatrix} \mathbf{E}_s^1(\omega_p^\beta) & \mathbf{E}_s^2(\omega_p^\beta) & \dots & \mathbf{E}_s^{3N}(\omega_p^\beta) \end{bmatrix}. \quad (8)$$

Accordingly, the signal subspace can be identified with a singular value decomposition procedure (that is, $\bar{\bar{\mathbf{K}}}(\omega_p^\beta) = \bar{\bar{\mathbf{U}}}(\omega_p^\beta) \bar{\bar{\mathbf{S}}}(\omega_p^\beta) \bar{\bar{\mathbf{V}}}(\omega_p^\beta)^H$), and the imaging functional over the interrogation domain \mathcal{D} at ω_p^β can be constructed as

$$\Psi_{nl}(\mathbf{r}, \omega_p^\beta, \Omega^\alpha) = \sum_{k=1}^3 \left(\sum_{l=L+1}^{3N} \left| \hat{\mathbf{u}}_l(\omega_p^\beta)^H \hat{\mathbf{g}}_k(\mathbf{r}^\alpha, \mathbf{r}, \omega_p^\beta) \right|^2 \right)^{-1}, \quad \mathbf{r} \in \mathcal{D} \subset \mathbb{R}^3, \quad (9)$$

with the assumption that the signal subspace is spanned by the first L singular vectors

$\hat{\mathbf{u}}_l(\omega_p^\beta)$ —which correspond to the first L significant singular values, and

$\hat{\mathbf{g}}_k(\mathbf{r}^\alpha, \mathbf{r}, \omega_p^\beta) = \mathbf{g}_k(\mathbf{r}^\alpha, \mathbf{r}, \omega_p^\beta) / \|\mathbf{g}_k(\mathbf{r}^\alpha, \mathbf{r}, \omega_p^\beta)\|$, where the vector $\mathbf{g}_k(\mathbf{r}^\alpha, \mathbf{r}, \omega_p^\beta)$ —generated as the asymptotic expressions from²⁷ (Appendix B) for computational efficiency purposes—is the

k -th column of $\left[\bar{\bar{\mathbf{G}}}_{\xi\eta}(\mathbf{r}, \mathbf{r}_1^\alpha, \omega_p^\beta) \quad \bar{\bar{\mathbf{G}}}_{\xi\eta}(\mathbf{r}, \mathbf{r}_2^\alpha, \omega_p^\beta) \quad \dots \quad \bar{\bar{\mathbf{G}}}_{\xi\eta}(\mathbf{r}, \mathbf{r}_N^\alpha, \omega_p^\beta) \right]^T$. The objective function in Equation 9 can also be computed and summed over multiple harmonics to enhance the stability of the algorithm.

As relevant to the linear scattering response, in the vector field case, note that each metallic point target would give rise to a maximum of three significant singular values (and associated singular vectors), and if the point targets are well-separated, each of these sets of singular values/vectors would have a one-to-one correspondence with the targets. An extended target, in contrast, could potentially give rise to more than three significant singular values/vectors. The imaging functional of the form in Equation 9 is expected to work well for both point and extended targets, since an extended target could be approximated as a collection of point radiators, each with a field pattern defined by $\bar{\bar{\mathbf{G}}}_{\xi\eta}(\cdot)$. To identify the null subspace needed in the imaging algorithm, the condition $3N > 3M$ —where M is the total *effective* number of individual scatterers in the scene—must be met. Additionally, as mentioned in other works,^{34,35} note that care must be taken in choosing the parameter L , especially in the presence of noise.

For the nonlinear scattering response, it is seen that each antenna scatterer—regardless of whether it can be treated as a point or extended target—has only one significant singular value/vector. This can be understood by noting that, in essence, the scattered field at each harmonic frequency $\omega_p^\beta \notin \Omega^\alpha$ is found by exciting the antenna terminal with voltage source $V_{ant}(\omega_p^\beta \in \Omega^\beta)$ —therefore, the receiver array is capturing the antenna radiation pattern and not the direct scattering response. As a consequence, without *a priori* knowledge of the harmonic radiation pattern, results from the imaging functional in Equation 9 may be degraded in some cases for the extended target scenario. To improve the imaging quality, the following composite imaging functional can be used:

$$\Psi(\mathbf{r}, \{\omega_p^\beta, \omega_q^\alpha\}, \Omega^\alpha) = \Psi_{nt}(\mathbf{r}, \omega_p^\beta, \Omega^\alpha) \cdot \Psi_l(\mathbf{r}, \omega_q^\alpha, \Omega^\alpha), \quad (10)$$

where the linear (or ordinary) scattering imaging result at excitation frequency ω_q^α is combined with the nonlinear (or harmonic) imaging result to isolate the nonlinear targets. Assuming there are M nonlinear targets in the scene, note that for the construction of the null subspace in the harmonic response case, the condition $3N > M$ needs to be satisfied.

3. Numerical Experiment Results

The framework put forth in Section 2 is first applied for analyzing the scattering and imaging responses of on-surface and subsurface nonlinearly loaded antenna targets in a half-space environment; then the complex-room detection problem is considered.

3.1 Sensing in Half-Space Environment

The employed sensing geometry is similar to that of the forward-looking radar system described in:^{19,22} the linear transceiver array is composed of $N = 16$ equally spaced elements distributed over a 2-m-wide aperture located at 2 m height. In the forward-looking direction, this sensing configuration offers resolution primarily in the down-range and cross-range extents; very limited depth resolution in the vertical extent is supported, even if field integration over multiple moving apertures is utilized. As such, the only localization parameters of interest are the down-range and cross-range positions of a target. In the first example, scenes consisting of nonlinearly loaded vertical dipole elements (50 cm in length) situated on the ground surface are considered. The ground soil is characterized by relative dielectric constant $\epsilon_r = 4$ and conductivity $\sigma = 15 \text{ mS/m}$. Figure 2a shows the scattered signal spectrum for a three-target scenario ($M = 3$) in which each antenna element is center-loaded with a diode: $i(t) = I_o \left(\exp(v(t)/v_i) - 1 \right)$, $I_o = 10 \text{ nA}$, $v_i = 26 \text{ mV}$; the bias network has parameters $R_b = 1 \text{ k}\Omega$, $V_b = 1 \text{ V}$. A single-tone excitation (with transmitted power of 4 W) at $f_1^\alpha = 300 \text{ MHz}$ is assumed, resulting in a scattered field spectrum composed of signals at multiples of the excitation frequency af_1^α ($a \in \{1, 2, \dots\}$). Note that only 10 harmonic frequency components ($|\Omega^\beta| = P = 10$) are computed in the harmonic balance solver. In this example (and in all that follow), the transmitter array is centered at $\mathbf{r} = (-10 \text{ m}, 2 \text{ m}, 2 \text{ m})$ and parallel to the y-axis. The singular value spectrum derived from the multistatic response at 600 MHz is illustrated in Fig. 3a, which shows the three dominant singular values corresponding to the targets. Images for the scene constructed with Equation 9 using the responses at frequencies 600 MHz, 900 MHz, 1500 MHz, and 2100 MHz are displayed in Fig. 4, where the true positions of the targets are also indicated. Simulation results for various levels of signal-to-noise ratio (SNR) from ∞ (no noise) to 10 dB are obtained and examined; the following definition for SNR is observed:

$$\text{SNR} = 20 \log_{10} \left(\left\| \bar{\mathbf{K}}(\omega_p^\beta) \right\|_F / \left\| \bar{\mathbf{N}}(\omega_p^\beta) \right\|_F \right), \quad (11)$$

in which $\bar{\mathbf{N}}(\omega_p^\beta)$ is a zero-mean Gaussian complex noise matrix, and $\|\cdot\|_F$ denotes the Frobenius norm operation. The interrogation domain here is $\mathcal{D} = \{\mathbf{r} = (x, y, z) \in \mathbb{R}^3 : -5 \text{ m} < x, y < 5 \text{ m}, -1 \text{ m} < z < 2 \text{ m}\}$, and the xy image slice that contains the maximum response

$$\Psi_{nl, \max} = \max_{\mathbf{r} \in \mathcal{D}} \left(\sum_{p=2,3,5,7} \Psi_{nl}(\mathbf{r}, \omega_p^\beta, \Omega^\alpha) \right) \quad (12)$$

is shown. As anticipated, the vertical resolution (in z) is very poor in this case; of primary interest is the imaging performance in the range and angular directions. (Throughout this work, the parameter L in the imaging functional is chosen by first plotting the singular value spectrum

in logarithmic scale and then identifying the “knee” point in the graph, which is taken as the demarcation between the signal and null subspaces.)

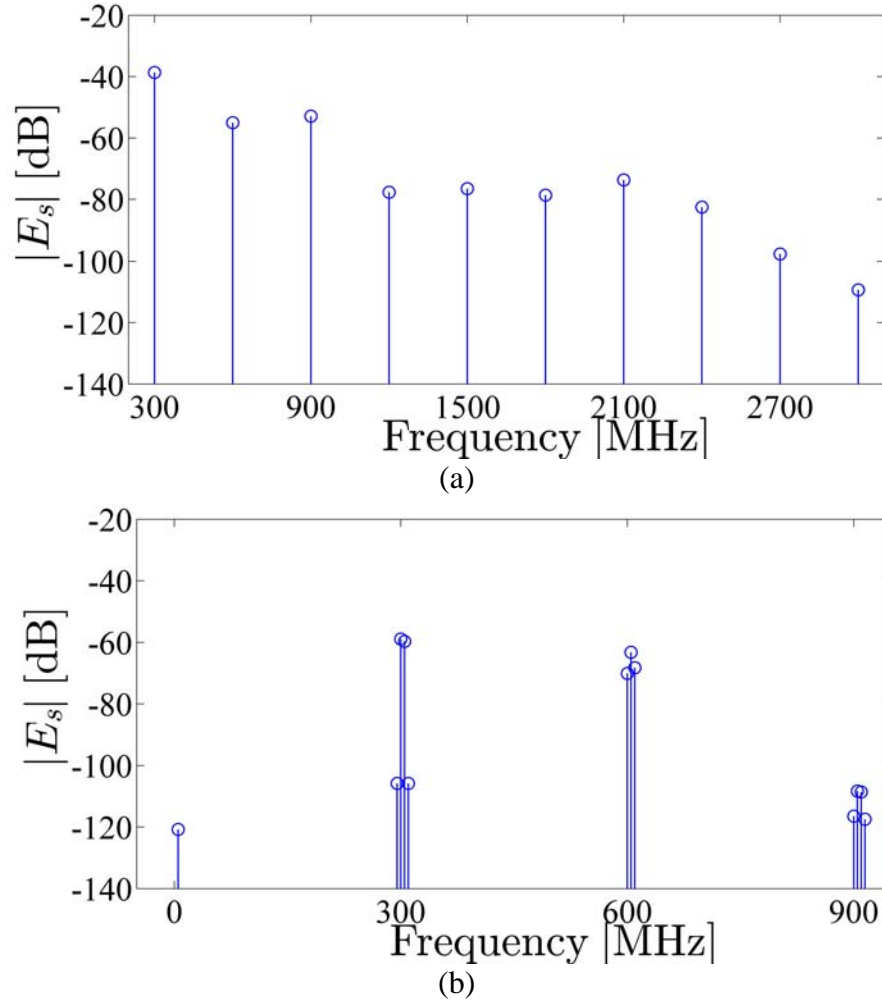


Fig. 2 Monostatic scattered electric field strength for center array element: a) Single-tone excitation at 300 MHz; three diode-loaded targets and b) Two-tone excitation at 300 MHz and 305 MHz; two varactor-loaded targets

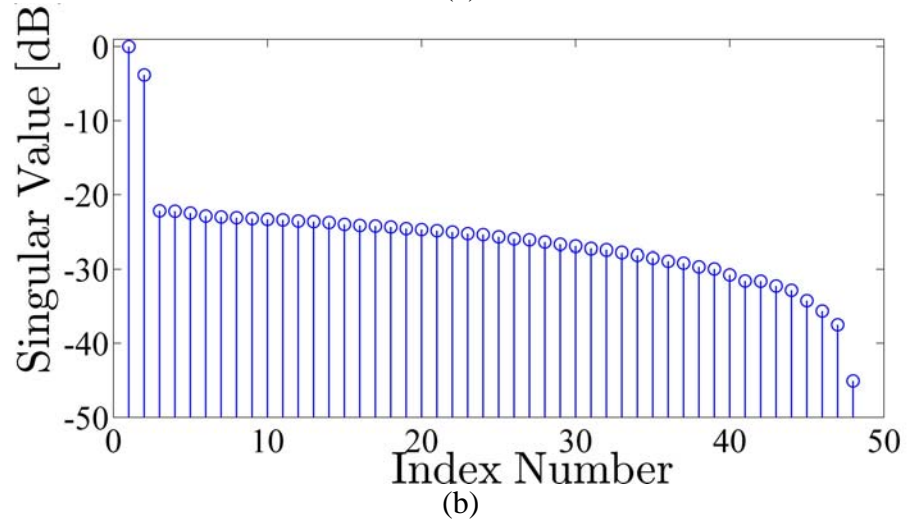
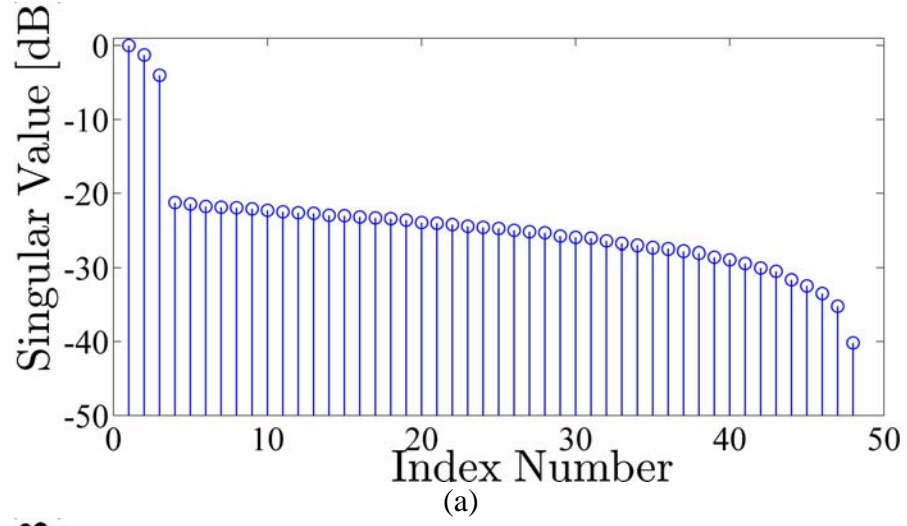


Fig. 3 Normalized singular value spectrum: a) Three diode-loaded targets and b) Two varactor-loaded targets

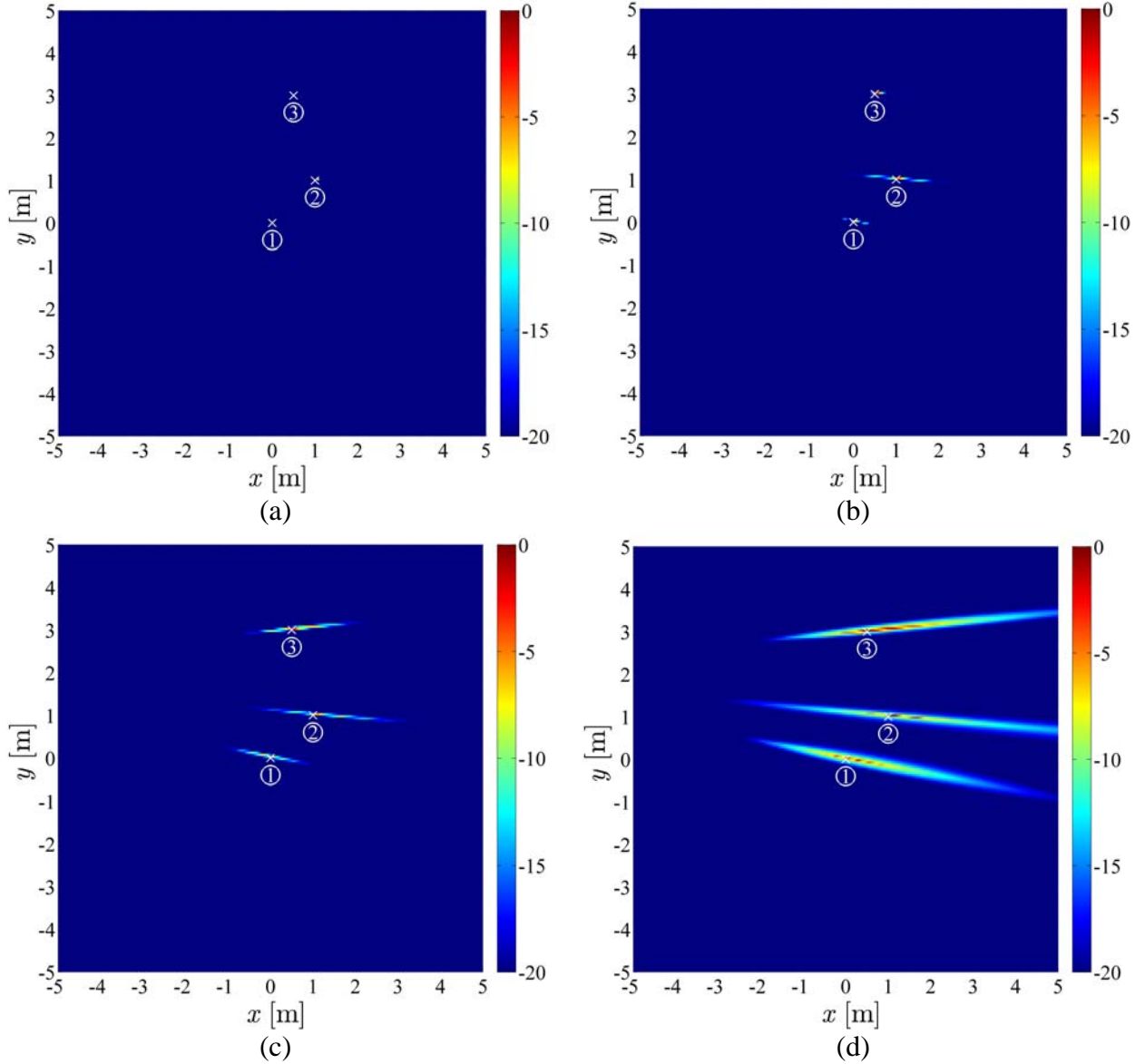


Fig. 4 Three diode-loaded vertical dipole antennas; single-tone excitation ($|\Omega^\alpha| = Q = 1$) at 300 MHz (transmitted power: 4 W). $|\Omega^\beta| = P = 10$. Imaging formation frequencies: 600 MHz, 900 MHz, 1500 MHz, 2100 MHz. a) SNR = ∞ (no noise); b) SNR = 30 dB; c) SNR = 20 dB; and d) SNR = 10 dB. Circled numbers denote nonlinear targets. The image intensity is displayed in dB scale.

As expected, the presence of the noise tends to degrade the resolution in both the range and angular directions; the range resolution, in particular, appears to be much more drastically affected. It is noted that under noiseless conditions, near perfect localization is seen—that is, as applicable to this example, the targets appear as near point responses in the image for SNR = ∞ (Fig. 4a). Specifically, the results not only show that the three targets are accurately localized but also numerically confirm the imaging method's potential in achieving super-resolution—which has been identified as one of the advantages of using a subspace-based method^{28,36}.

It should be emphasized that the reason for adopting the particular aspect-limited aperture with the prescribed array parameters is to conform to the operational constraints of a ground-based, forward-looking system. The application of a larger linear aperture (or a full aperture) may improve the imaging performance; for example, as applied to the traditional linear scattering response, full circular arrays have been considered in,^{37–39} where only 2D problems are treated. From the implementation perspective, however, large aperture- and circular aperture-based sensing configurations—commonly used in other studies—are not practical for the current application.

To investigate the decay rates of the harmonic signal intensities in terms of sensing distance, the scattered fields are computed and plotted as a function of standoff range, ρ , or the radial separation between the observation point and a target. As a generalization, with small-signal analysis, it is demonstrated that—for the backscattering-based sensing scenario in which the interaction points are positioned close to the ground surface—the amplitude of each harmonic order of the scattered field, in the asymptotic propagation regime, approximately depends on the distance as $\propto \rho^{-2(a+1)}$; this behavior is consistent with theoretical results derived using analytical models for the nonlinear circuit response and field propagation.²³ Thus, the nonlinear scattered components experience faster decay rates as compared to the conventional $\propto \rho^{-4}$ factor encountered in linear radar analysis; this propagation characteristic has to be considered in assessing the link budget in the design of the sensing system.

The scattering and imaging results for a 2-target scenario are displayed in Figs. 2b and 5. In this case, each vertical dipole antenna is center-loaded with a varactor:

$i(t) = C_{jo} \left(1 + v(t)/v_{bi}\right)^{-\gamma} \cdot dv(t)/dt$, $C_{jo} = 2$ pF, $v_{bi} = 0.7$ V, $\gamma = 0.5$; the bias network has parameters $R_b = 1$ k Ω , $V_b = 0.1$ V. A 2-tone excitation (with transmitted power of 1.7 W) at $f_1^\alpha = 300$ MHz and $f_2^\alpha = 305$ MHz is considered, which results in a scattering spectrum consisting of responses at $af_1^\alpha + bf_2^\alpha$, where a and b are integers. Note that only 12 harmonic frequency components ($|\Omega^\beta| = P = 12, |a| + |b| \leq 3$) are computed in the harmonic balance solver.

The singular value spectrum at 600 MHz is shown in Fig. 3b. The image is generated using the multistatic scattered signal at frequencies 600 MHz, 605 MHz, and 610 MHz. The decay rate of the harmonic scattered components in this case is seen to be of the form $\propto \rho^{-2(|a|+|b|+1)}$.

Consequently, the *relative* strengths of the various spectral components compared to each other are distance dependent: for example, although the 5 MHz ($a = -1, b = 1$) component is weaker than the 295 MHz ($a = 2, b = -1$) and 310 MHz ($a = -1, b = 2$) components in the near range ($\rho \approx 10$ m), it may become the stronger component at longer ranges. The main gist of these observations can be generalized to the multi-tone excitation configuration.

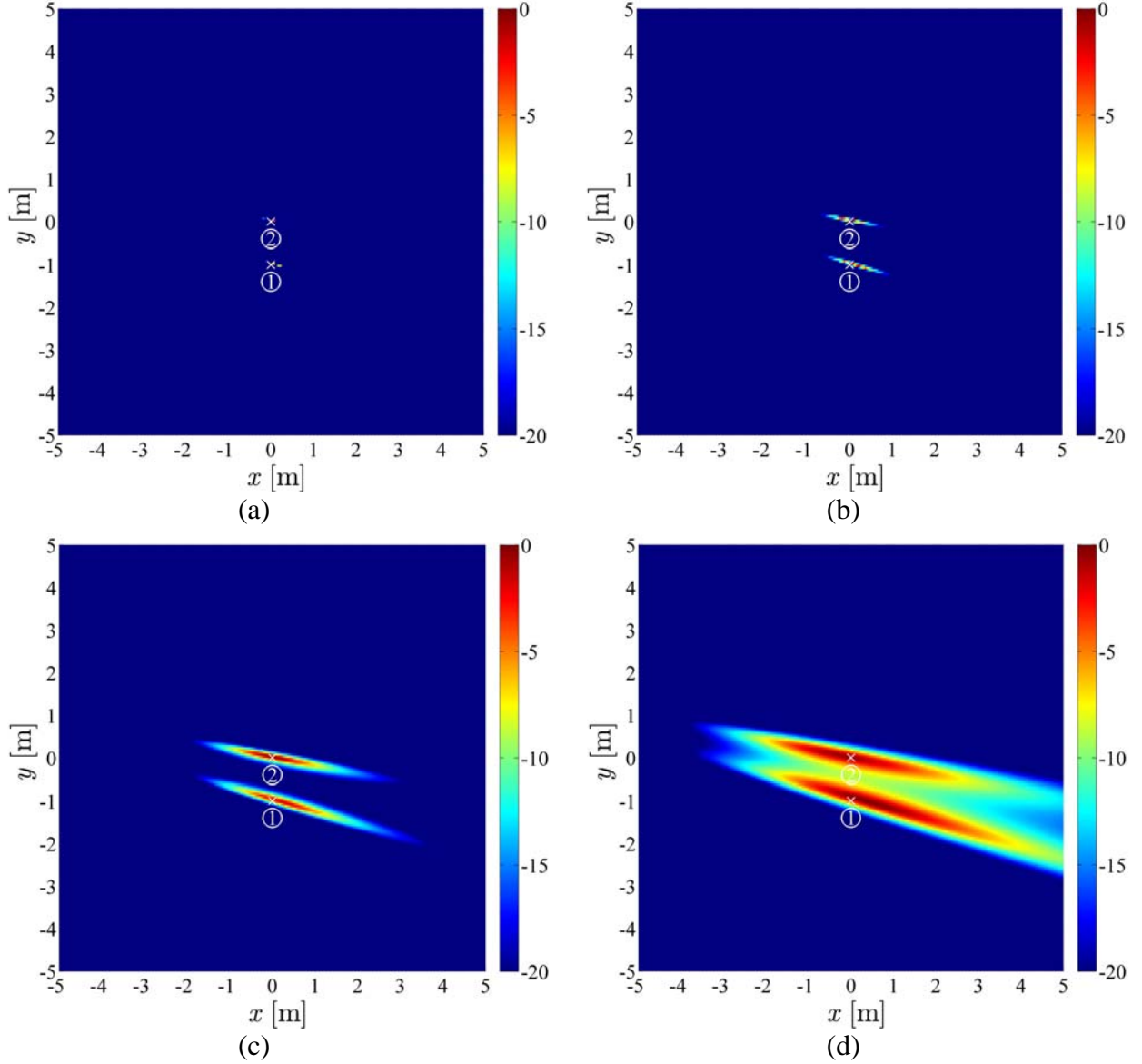


Fig. 5 Two varactor-loaded vertical dipole antennas; double-tone excitation ($|\Omega^\alpha| = Q = 2$) at 300 MHz and 305 MHz (transmitted power: 1.7 W). $|\Omega^\beta| = P = 12$. Imaging formation frequencies: 600 MHz, 605 MHz, 610 MHz. a) SNR = ∞ (no noise); b) SNR = 30 dB; c) SNR = 20 dB; and d) SNR = 10 dB.

The scenarios considered in Fig. 6 are similar to those in Figs. 4 and 5, with the only difference being that one of the antenna elements is treated as a purely linear clutter object: in Fig. 6a, scatterers 1 and 3 are diode-loaded, whereas scatterer 2 has no nonlinear loading (i.e., in this case, the antenna is short-circuited at its feeding terminal); in Fig. 6b, scatterer 1 is varactor-loaded whereas scatterer 2 is short-circuited. The images show that the nonlinear targets are all identified. (For space considerations, henceforth only the results for SNR = 20 dB are included here.) It should be mentioned that, for the simulation parameters and the set of inter-target

separation distances considered in this example, inter-scatterer coupling effects are negligible; for smaller separation distances, however, it is possible that these coupling effects could become important—for instance, the re-radiation from the nonlinear scatterer could induce harmonic currents on the linear clutter object, which in turn would radiate responses at the harmonic frequencies even though it inherently behaves as a purely linear scatterer.

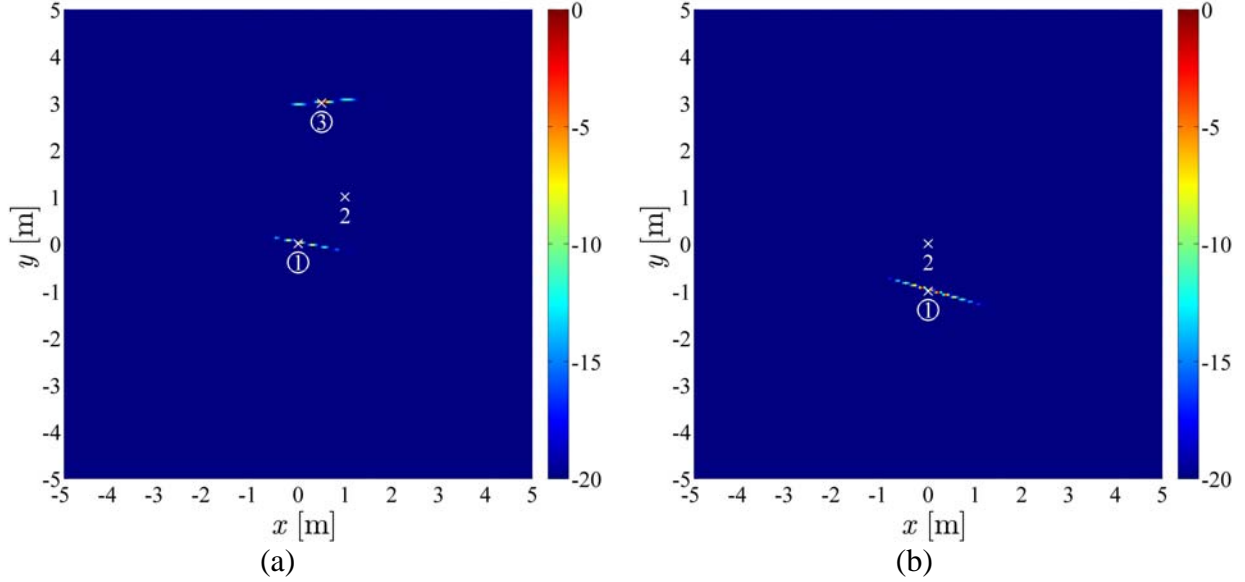


Fig. 6 Same scenarios as those in Figs. 4 and 5, except scatterer 2 is a linear clutter object. SNR = 20 dB

In the next example, scattering from horizontal dipole antennas (50 cm in length) situated directly on top of the ground surface is simulated. For the scenes corresponding to the images in Fig. 7, all the targets are nonlinear except for scatterer 2 in Fig. 7b, which is short-circuited. Nonlinearly loaded targets are center-loaded with a diode that has the same parameters as those in the previous cases. It is seen that the radiation modes from the horizontal dipole antenna are not as *well approximated* by $\bar{\bar{G}}_{\xi\eta}(\cdot)$ as those from the previously considered vertical dipoles; thus, the imaging ansatz in Equation 9 is applied to improve the localization performance. Specifically, single-tone excitation at 300 MHz is assumed, and the fundamental and second harmonic returns are captured at the receiver array. Once again, the “spreading” of the target image response in the range direction is primarily due to the presence of noise.

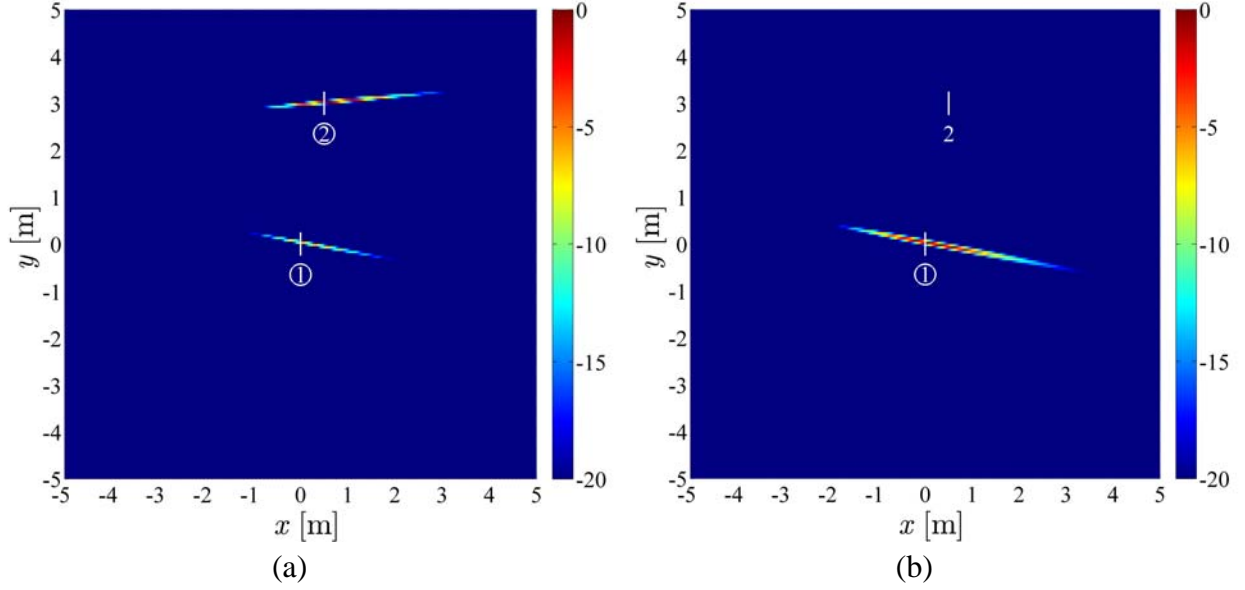


Fig. 7 a) Two diode-loaded horizontal dipole antennas and b) One diode-loaded horizontal dipole antenna (scatterer 1) and one linear clutter object (scatterer 2). Single-tone excitation ($|\Omega^\alpha| = Q = 1$) at 300 MHz (transmitted power: 4 W). $|\Omega^\beta| = P = 10$. Imaging formation frequencies: 300 MHz, 600 MHz, and SNR = 20 dB.

In the last example, the nonlinear targets are embedded in a clutter field: the 2 diode-loaded horizontal dipole antenna targets (scatterers 1 and 4) are either located on the ground surface (Fig. 8a) or buried in the ground at 3 cm depth (Fig. 8b); the linear surface clutter objects consist of small metallic cylinders and short-circuited dipoles of different orientations. The imaging functional in equation 9 is applied with single-tone excitation and fundamental scattering observation at 300 MHz, and harmonic scattering observation at 1200 MHz. The images indicate that the nonlinear targets are detected with good angular resolution—albeit the range resolution is degraded because of the addition of noise to the scattering response.

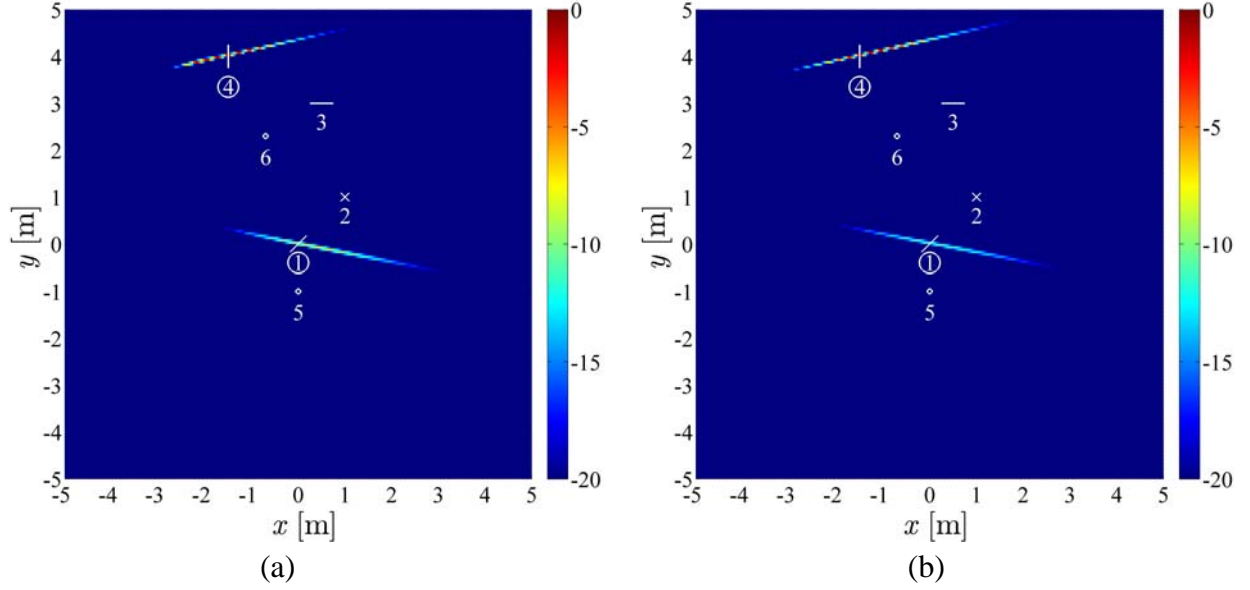


Fig. 8 Two diode-loaded horizontal dipole antennas (scatterers 1 and 4) in a clutter field: a) On-surface and b) Buried. Scatterer 2 is a vertical dipole; scatterer 3 is a horizontal dipole; scatterers 5 and 6 are metallic cylinders. Single-tone excitation ($|\Omega^\alpha| = Q = 1$) at 300 MHz (transmitted power: 4 W). $|\Omega^\beta| = P = 10$. Imaging formation frequencies: 300 MHz, 1200 MHz, and SNR = 20 dB.

3.2 Sensing in Complex-Room Environment

Localization of a nonlinearly loaded antenna target is considered with the sensing configuration shown in Figs. 9a, 10a, and 11a. The electrical properties of all the structures and objects (walls, ceiling, floor, furniture, humans, etc.) found within the complex room scene are described in;⁴⁰ the transceiver array is similar to the one used in Section 3.1, except that here it is centered at $\mathbf{r} = (6.5 \text{ m}, 0 \text{ m}, 2 \text{ m})$; and the target—centered at 1 m height—is the same diode-loaded vertical dipole antenna that was previously noted. The procedure for scattering characterization closely follows the one outlined in Section 2.1, with field propagation to and from the target computed using a finite-difference time-domain solver.⁴⁰ As the exact Green's function for this environment is complicated and cannot be readily derived, one key approximation is made to facilitate the analysis: for both the integral equation solver and the image generation, the half-space Green's function is assumed. The imaging results for three target positions are displayed in Figs. 9b, 10b, and 11b: in all cases, a single-tone excitation at $f_1^\alpha = 300 \text{ MHz}$ is employed, and the images are constructed using the responses at 600 MHz. It is seen that while the cross-range resolution is satisfactory, the range resolution is rather poor. The degradation in range resolution—as well as in range positioning accuracy—is primarily due to the presence of the front wall and the in-room clutter in the vicinity of the target—the effects of both of which are not taken into account in the imaging construction, given that only the half-space Green's function is applied within the imaging functional Equation 9.

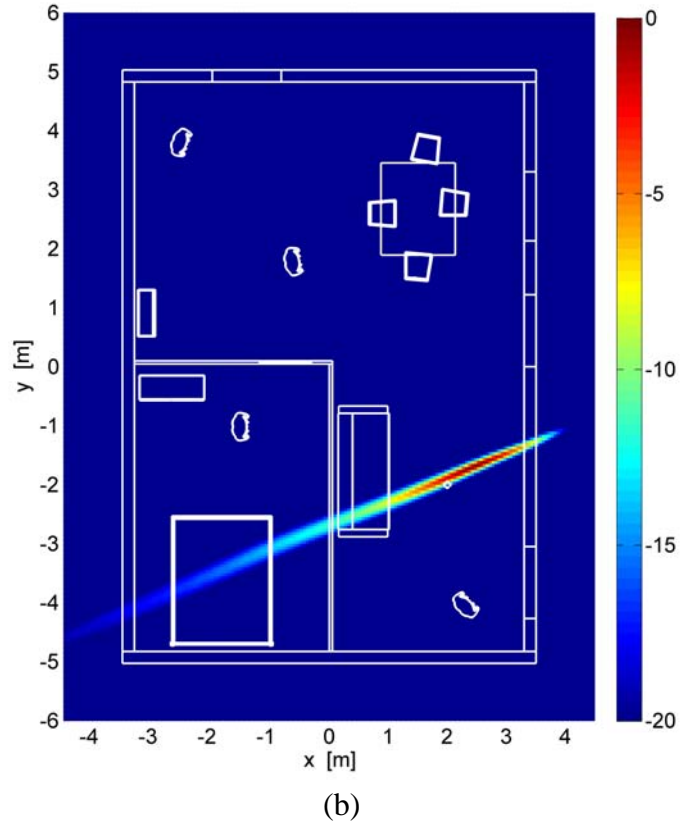
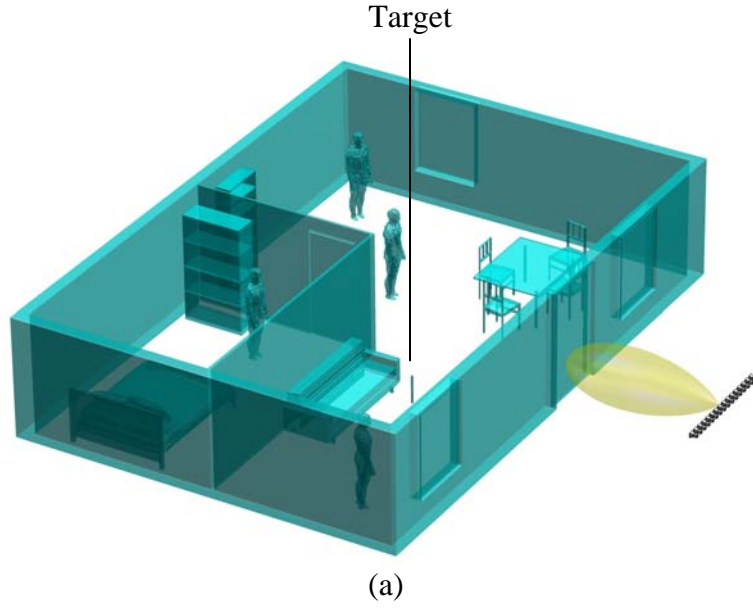


Fig. 9 a) Diode-loaded dipole antenna in a complex-room environment—position 1 and b) Imaging result with single-tone excitation ($|\Omega^\alpha| = Q = 1$) at 300 MHz (transmitted power: 4 W). $|\Omega^\beta| = P = 10$. Imaging formation frequency: 600 MHz, SNR = 20 dB.

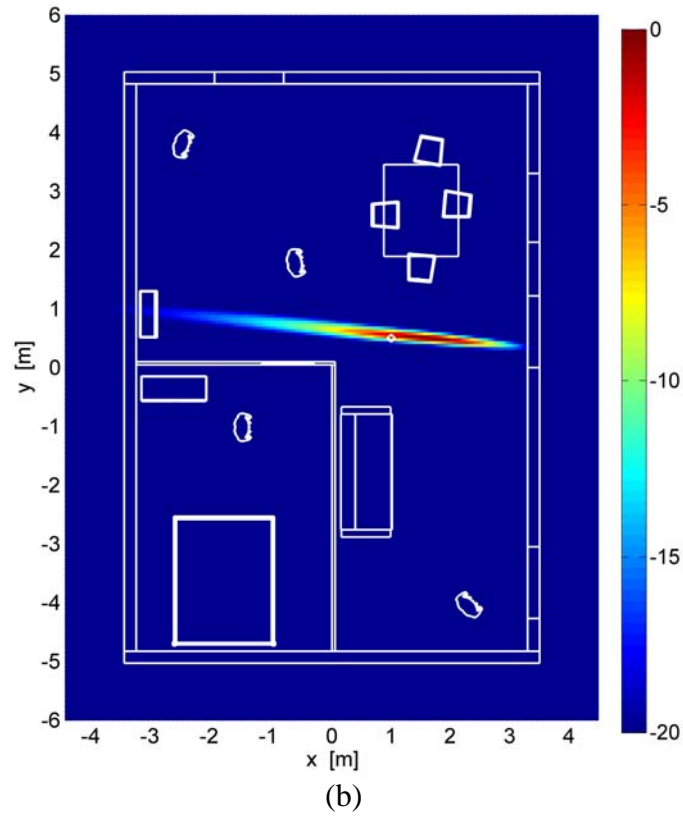
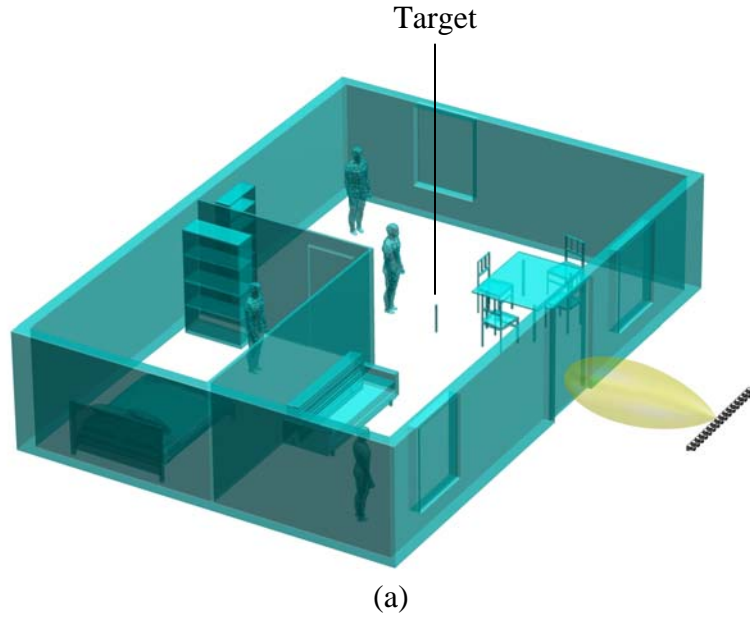


Fig. 10 a) Diode-loaded dipole antenna in a complex-room environment—position 2 and b) Imaging result with single-tone excitation ($|\Omega^a| = Q = 1$) at 300 MHz (transmitted power: 4 W). $|\Omega^b| = P = 10$. Imaging formation frequency: 600 MHz, SNR = 20 dB.

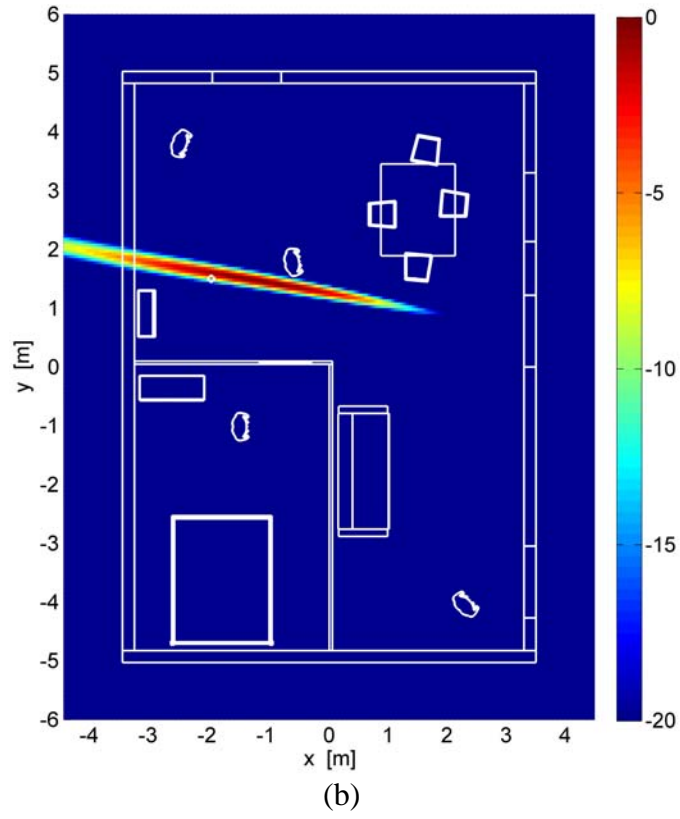
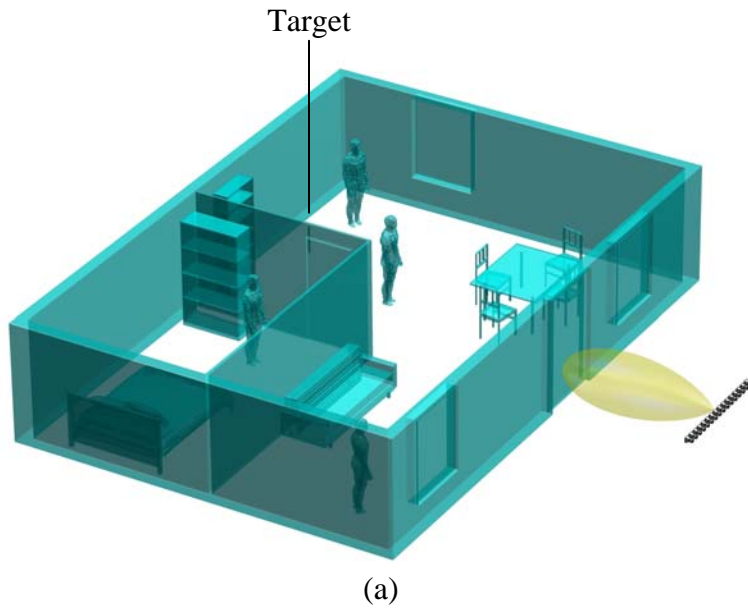


Fig. 11 a) Diode-loaded dipole antenna in a complex-room environment—position 3 and b) Imaging result with single-tone excitation ($|\Omega^\alpha| = Q = 1$) at 300 MHz (transmitted power: 4 W). $|\Omega^\beta| = P = 10$. Imaging formation frequency: 600 MHz, SNR = 20 dB.

4. Conclusions

To facilitate the development of a complementary nonlinear detection capability for an existing near-ground, forward-looking linear imaging radar system, a numerical solver is presented in this work for characterizing the multiview, multistatic RF harmonic response of nonlinearly loaded antenna targets under tone excitation—viz., a half-space method-of-moments approach is applied for deriving the equivalent circuit of the antenna structure; the harmonic balance technique is employed in solving for the steady-state response of the nonlinear system; and asymptotic methods are adapted when appropriate in the propagation and scattering routines to characterize the re-radiation modes of the scatterer. Additionally, a subspace-based direct imaging technique is developed and demonstrated for near-field location estimation of on-surface and buried targets. An extensive set of numerical experiments has been carried out, and scattering and imaging results have been derived for sensing scenarios with and without linear clutter. The imaging responses indicate that by using an aspect-limited transceiver aperture consistent with that of the aforementioned forward-looking radar, accurate target localization can be obtained. In sum, the harmonic detection technique is observed to be a viable method for isolating nonlinearly loaded targets from surrounding linear surface clutter in a sparse scene; however, the imaging performance is determined to be rather noise sensitive—with the down-range resolution being much more vulnerable to noise effects than the angular resolution; the practicality of nonlinear sensing is also limited to the near range due to the higher-order attenuation rates of the harmonic backscattered fields. Although the focus of the study is on the half-space problem, target localization and imaging in a complex-room environment are also considered. It is seen that the use of an approximate Green's function (e.g., the half-space formulation) in lieu of an exact formulation in the imaging objective function can—as expected—lead to degradation in the range resolution and positioning accuracy, whereas the angular resolution and positioning accuracy are less affected.

Note that the electromagnetic scattering and imaging approaches presented herein can be extended for the treatment of wideband sensing scenarios. For example, the targets can be excited by multiple, separate sets of tones in a sequential manner, and then the imaging functional is integrated over all harmonic response sets to enhance the detection performance. A moving transceiver aperture configuration could also provide multiple independent scattering responses needed to further improve the accuracy of the localization scheme. These issues will be investigated in future studies.

5. References

1. Harger RO. Harmonic radar systems for near-ground in-foliage nonlinear scatterers. *IEEE Trans Aerosp Electron Syst.* 1976;12:230–245.
2. Anderson SJ. Nonlinear scattering at HF: Prospects for exploitation in OTH radar systems. *Turk J Elec Eng Comp Sci.* 2010;18:439–456.
3. Schuman HK. Time-domain scattering from a nonlinearly loaded wire. *IEEE Trans Antennas Propagat.* 1974;22:611–613.
4. Liu TK, Tesche FM. Analysis of antennas and scatterers with nonlinear loads. *IEEE Trans Antennas Propagat.* 1976;24:131–139.
5. Landt JA, Miller EK, Deadrick FJ. Time domain modeling of nonlinear loads. *IEEE Trans Antennas Propagat.* 1983;31:121–126.
6. Porti JA, Morente JA. A numerical analysis of wire antennas loaded with varistor-composite materials. *IEEE Trans Electromagn. Compat.* 1994;36:23–31.
7. Sarkar TK, Weiner DD. Scattering analysis of nonlinearly loaded antennas. *IEEE Trans Antennas Propagat.* 1976;24:125–131.
8. Huang C-C, Chu T-H. Analysis of wire scatterers with nonlinear or time-harmonic loads in the frequency domain. *IEEE Trans Antennas Propagat.* 1993;41:25–30.
9. Lee KC. An efficient algorithm for the steady-state analysis of a nonlinearly loaded antenna array. *J Electromagn Waves Applicat.* 2000;14:1373–1382.
10. Lee KC. Analysis of large nonlinearly loaded antenna arrays under multitones excitation. *Microw Opt Technol Lett.* 2000;25:319–323.
11. Lee KC. Two efficient algorithms for the analyses of a nonlinearly loaded antenna and antenna array in the frequency domain. *IEEE Trans Electromagn. Compat.* 2000;45:339–346.
12. Lee KC. Genetic algorithms based analyses of nonlinearly loaded antenna arrays including mutual coupling effects. *IEEE Trans Antennas Propagat.* 2003;51:776–781.
13. Sarkar TK, Weiner DD, Harrington RF. Analysis of nonlinearly loaded multiport antenna structures over an imperfect ground plane using the Volterra-series method. *IEEE Trans Electromagn Compat.* 1978;20:278–287.
14. Poljak D, Tham CY, McCowen A. Transient response of nonlinearly loaded wires in a two media configuration. *IEEE Trans Electromagn Compat.* 2004;46:121–125.

15. Sheshyekani K, Sadeghi SHH, Moini R. A combined MoM-AOM approach for frequency domain analysis of nonlinearly loaded antennas in the presence of a lossy ground. *IEEE Trans Antennas Propagat.* 2008;56:1717–1724.
16. Karami HR, Moini R, Sadeghi SHH, Sheshyekani K. Transient response of nonlinearly loaded antennas above a lossy dielectric half-space: A modified MoM-AOM approach. *IEEE Trans Electromagn. Compat.* 2012;54:922–930.
17. Borcea L, Papanicolaou G, Tsogka C. A resolution study for imaging and time reversal in random media. *Cont Mathem.* 2003;333:63–77.
18. Sarabandi K, Koh I, Cusiato M. Demonstration of time reversal methods in a multi-path environment. *Proc. IEEE Antennas and Propagat Soc Symp.*; 2004.
19. Liao DH, Dogaru T. Full-wave characterization of rough terrain surface scattering for forward-looking radar applications. *IEEE Trans Antennas Propagat.* 2012;60:3853–3866.
20. Mascanzoni D, Wallin H. The harmonic radar: A new method of tracing insects in the field. *Eco Ent.* 1986;11:387–390.
21. Tahir N, Brooker G. Recent developments and recommendations for improving harmonic radar tracking systems. *Proc. 5th Euro Conf Antennas Propagat.*; 2011.
22. Ressler M, Nguyen L, Koenig F, Wong D, Smith G. The ARL synchronous impulse reconstruction (SIRE) forward-looking radar. *Proc SPIE*; 2007;6561.
23. Liao DH. A hybrid approach for characterizing linear and nonlinear electromagnetic scattering: theory and applications. Adelphi (MD): Army Research Laboratory (US); November 2012. Report No.: ARL-TR-6261.
24. Tsang L, Kong JA, Shin R.T. Theory of microwave remote sensing. New York (NY): Wiley-Interscience; 1985.
25. Liao DH, Sarabandi K. Terminal-to-terminal hybrid full-wave simulation of low-profile, electrically-small, near-ground antennas. *IEEE Trans. Antennas Propagat.* 2008;56:806–814.
26. Liao DH, Sarabandi K. Near-earth wave propagation characteristics of electric dipole in presence of vegetation or snow layer. *IEEE Trans. Antennas Propagat.* 2005;53:3747–3756.
27. Liao DH. Physics-based near-earth radiowave propagation modeling and simulation [PhD dissertation]. [City (state abbreviation)]: The University of Michigan; 2009.
28. Lev-Ari H, Devaney AJ. The time-reversal technique reinterpreted: subspace-based signal processing for multi-static target location. *Proc. IEEE Sensor Array and Multichannel Sig. Proc. Workshop*; 2000.

29. Devaney AJ. Time reversal imaging of obscured targets from multistatic data. *IEEE Trans Antennas Propagat.* 2005;53:1600–1610.
30. Devaney AJ, Marengo EA, Gruber FK. Time-reversal-based imaging and inverse scattering of multiply scattering point targets. *J Acoust Soc Am.* 2005;118:3129–3138.
31. Gruber FK, Marengo EA, Devaney AJ. Time-reversal imaging with multiple signal classification considering multiple scattering between the targets. *J Acoust Soc Am.* 2004;115:3042–3047.
32. Liu X-F, Wang B-Z, Xiao S-Q. Electromagnetic subsurface detection using subspace signal processing and half-space dyadic green's function. *Prog Electromagn Res.* 2009;98:315–331.
33. Zhang W, Hoorfar A, Li L. Through-the-wall target localization with time reversal MUSIC method. *Prog Electromagn Res.* 2010;106:75–89.
34. Marengo EA, Gruber FK, Simonetti F. Time-reversal MUSIC imaging of extended targets. *IEEE Trans Image Process.* 2007;16:1967–1984.
35. Hou S, Solna K, Zhao H. A direct imaging algorithm for extended targets. *Inv Probl* 2006;22:1151–1178.
36. Davy M, Minonzio J-G, de Rosny J, Prada C, Fink M. Influence of noise on subwavelength imaging of two close scatterers using time reversal method: Theory and experiments. *Prog Electromagn Res.* 2009;98:333–358.
37. Agarwal K, Chen X. Applicability of MUSIC-type imaging in two-dimensional electromagnetic inverse problems. *IEEE Trans Antennas Propagat.* 2008;56:3217–3223.
38. Chen X. Multiple signal classification method for detecting point-like scatterers embedded in an inhomogeneous background medium. *J Acoust Soc Am.* 2010;127:2392–2397.
39. Zhang G, Wang WW, Wang W. Energy estimation based TR-MUSIC microwave imaging for extended targets. *Prog Electromagn Res B* 2013;47:107–126.
40. Dogaru T, Liao DH, Le C. Three-dimensional radar imaging of a building. Adelphi (MD): Army Research Laboratory (US); December 2012. Report No.: ARL-TR-6295.

Appendix A. Variable Definitions for Section 2.1

The following definitions are needed for Equation 1:

$$\mathbf{V}_{ant} \in \mathbb{R}^{(2P+1) \times 1} = \begin{bmatrix} V_{ant,DC} & V_{ant,1} & V_{ant,2} & \cdots & V_{ant,2P-1} & V_{ant,2P} \end{bmatrix}^T; \quad (\text{A-1})$$

the elements of $\mathbf{I}_{sc} \in \mathbb{R}^{(2P+1) \times 1}$ are only nonzero at the excitation frequency components ω_q^α :

$$\mathbf{I}_{sc} \big|_{\omega_q^\alpha} = \begin{bmatrix} I_{sc,2q-1} & I_{sc,2q} \end{bmatrix}^T; \quad (\text{A-2})$$

the antenna admittance matrix is

$$\bar{\bar{\mathbf{Y}}}_{ant} \in \mathbb{R}^{(2P+1) \times (2P+1)} = \begin{bmatrix} 0 & 0 & 0 & \cdots & & 0 \\ 0 & G(\omega_1^\beta) & B(\omega_1^\beta) & & & \\ 0 & -B(\omega_1^\beta) & G(\omega_1^\beta) & & & \\ \vdots & & & G(\omega_2^\beta) & B(\omega_2^\beta) & \\ & & & -B(\omega_2^\beta) & G(\omega_2^\beta) & \\ & & & & \ddots & \\ & & & & & G(\omega_p^\beta) & B(\omega_p^\beta) \\ & & & & & -B(\omega_p^\beta) & G(\omega_p^\beta) \\ 0 & & & & & & \end{bmatrix}, \quad (\text{A-3})$$

with $G(\omega_p^\beta) = \Re(Y_{ant}(\omega_p^\beta))$ and $B(\omega_p^\beta) = \Im(Y_{ant}(\omega_p^\beta))$.

Denoting the temporal sampling rate as δt and the total number of time steps as N_t , the transformation matrices can be shown to be

$$\bar{\bar{\mathbf{T}}}_{t \leftarrow f} \in \mathbb{R}^{N_t \times (2P+1)} = \begin{bmatrix} 1 & \cos(\omega_1^\beta \cdot 0\delta t) & \sin(\omega_1^\beta \cdot 0\delta t) & \cdots & \cos(\omega_p^\beta \cdot 0\delta t) & \sin(\omega_p^\beta \cdot 0\delta t) \\ 1 & \cos(\omega_1^\beta \cdot 1\delta t) & \sin(\omega_1^\beta \cdot 1\delta t) & \cdots & \cos(\omega_p^\beta \cdot 1\delta t) & \sin(\omega_p^\beta \cdot 1\delta t) \\ \vdots & \vdots & \vdots & \ddots & \vdots & \vdots \\ 1 & \cos(\omega_1^\beta \cdot (N_t-1)\delta t) & \sin(\omega_1^\beta \cdot (N_t-1)\delta t) & \cdots & \cos(\omega_p^\beta \cdot (N_t-1)\delta t) & \sin(\omega_p^\beta \cdot (N_t-1)\delta t) \end{bmatrix}, \quad (\text{A-4})$$

and $\bar{\bar{\mathbf{T}}}_{f \leftarrow t} \in \mathbb{R}^{(2P+1) \times N_t} = \left(\bar{\bar{\mathbf{T}}}_{t \leftarrow f}^T \bar{\bar{\mathbf{T}}}_{t \leftarrow f} \right)^{-1} \bar{\bar{\mathbf{T}}}_{t \leftarrow f}^T$.

In accordance with the $i-v$ characteristics employed in Section 3, the Jacobian of the left hand side of Equation 1 with respect to \mathbf{V}_{ant} is derived as

$$\bar{\bar{\mathcal{J}}}(\mathbf{V}_{ant}) = \bar{\bar{\mathbf{T}}}_{f \leftarrow t} \cdot \text{diag} \left(\left. \frac{di(t)}{dv(t)} \right|_{V_{ant}(t)} \right) \cdot \bar{\bar{\mathbf{T}}}_{t \leftarrow f} + \bar{\bar{\mathbf{Y}}}_{ant} + \frac{1}{R_b} \bar{\bar{\mathbf{H}}} \quad (\text{A-5})$$

for a diode, and

$$\begin{aligned} \bar{\bar{\mathcal{J}}}(\mathbf{v}_{ant}) = & \bar{\bar{\mathbf{T}}}_{f \leftarrow t} \\ & \cdot \left[\text{diag} \left(\frac{dv(t)}{dt} \Big|_{\substack{V_{ant}(t) \\ \forall t=n_t \delta t}} \right) \cdot \text{diag} \left(\frac{dc(v(t))}{dv(t)} \Big|_{\substack{V_{ant}(t) \\ \forall t=n_t \delta t}} \right) \cdot \bar{\bar{\mathbf{T}}}_{t \leftarrow f} + \text{diag} \left(c(v(t)) \Big|_{\substack{V_{ant}(t) \\ \forall t=n_t \delta t}} \right) \cdot \bar{\bar{\mathbf{T}}}_{t \leftarrow f} \cdot \bar{\bar{\boldsymbol{\omega}}} \cdot \bar{\bar{\mathbf{S}}} \right] + \bar{\bar{\mathbf{Y}}}_{ant} + \frac{1}{R_b} \bar{\bar{\mathbf{H}}} \end{aligned} \quad (\text{A-6})$$

for a varactor, in which $n_t \in \{0, 1, \dots, N_t - 1\}$, $c(v(t)) = C_{jo} \left(1 + v(t)/v_{bi}\right)^{-\gamma}$, and

$$\bar{\bar{\boldsymbol{\omega}}} \in \mathbb{R}^{(2P+1) \times (2P+1)} = \text{diag} \left(\begin{bmatrix} 0 & \omega_1^\beta & \omega_1^\beta & \omega_2^\beta & \omega_2^\beta & \dots & \omega_p^\beta & \omega_p^\beta \end{bmatrix} \right); \quad (\text{A-7})$$

$$\bar{\bar{\mathbf{S}}} \in \mathbb{R}^{(2P+1) \times (2P+1)} = \begin{bmatrix} 0 & 0 & \dots & & 0 \\ 0 & 0 & 1 & & \\ \vdots & -1 & 0 & & \\ & & & 0 & 1 \\ & & & -1 & 0 \\ 0 & & & & \ddots \end{bmatrix}. \quad (\text{A-8})$$

INTENTIONALLY LEFT BLANK.

Appendix B. Asymptotic Green's Function Definitions for Half-Space

Closed-form analytical expressions for $\bar{\bar{\mathbf{G}}}_{\xi\eta}(\cdot)$ are derived from exact Sommerfeld integrals using the method of steepest descents. Based on the near-ground sensing geometry presented herein, using the notational convention from,²⁶ $\bar{\bar{\mathbf{G}}}_{\xi\eta}(\cdot) = \bar{\bar{\mathbf{G}}}_{00}(\cdot) = \bar{\bar{\mathbf{G}}}_{fs}(\cdot) + \bar{\bar{\mathbf{G}}}_r(\cdot)$ for on-surface targets and $\bar{\bar{\mathbf{G}}}_{\xi\eta}(\cdot) = \bar{\bar{\mathbf{G}}}_{01}(\cdot) = \bar{\bar{\mathbf{G}}}_t(\cdot)$ for buried targets, where $\bar{\bar{\mathbf{G}}}_{fs}(\cdot)$ is the free-space wave component. By following the derivation outlined in,²⁶ for an infinitesimal electric current element located on the z -axis at z' and an observation point at $\mathbf{r} = (\rho, \phi, z)$, it can be shown that the second-order-accurate ground wave components $\bar{\bar{\mathbf{G}}}_r(\cdot)$ and $\bar{\bar{\mathbf{G}}}_t(\cdot)$ are given by

$$\bar{\bar{\mathbf{G}}}_{r,t}(\cdot) = -\frac{\omega u_o k_o^2}{8\pi} e^{ik_o r} \cdot \left[\bar{\bar{\mathbf{F}}}_{r,t}(w_s) \left(\frac{1}{ik_o} \right) \left(\frac{1}{\rho^{1/2} r^{1/2}} \right) + \frac{1}{2} \left(\bar{\bar{\mathbf{F}}}_{r,t}''(w_s) + \frac{1}{4} \bar{\bar{\mathbf{F}}}_{r,t}(w_s) \right) \left(\frac{1}{ik_o} \right)^2 \left(\frac{1}{\rho^{1/2} r^{3/2}} \right) \right], \quad (\text{B-1})$$

with

$$\bar{\bar{\mathbf{F}}}_r(w) = \begin{bmatrix} \sin^{\frac{1}{2}} w \cos w m_{r,-}(w) & -\sin^{\frac{1}{2}} w \cos w r_+(w) \sin(2\phi) & -\frac{2}{k_o} \sin^{\frac{3}{2}} w \cos w r_v(w) \cos \phi \\ -\sin^{\frac{1}{2}} w \cos w r_+(w) \sin(2\phi) & \sin^{\frac{1}{2}} w \cos w m_{r,+}(w) & -\frac{2}{k_o} \sin^{\frac{3}{2}} w \cos w r_v(w) \sin \phi \\ \frac{2}{k_o} \sin^{\frac{3}{2}} w \cos w r_v(w) \cos \phi & \frac{2}{k_o} \sin^{\frac{3}{2}} w \cos w r_v(w) \sin \phi & \frac{2}{k_o} \sin^{\frac{5}{2}} w r_v(w) \end{bmatrix}; \quad (\text{B-2})$$

$$\bar{\bar{\mathbf{F}}}_t(w) = e^{ik_o(\epsilon_r - \sin^2 w)^{1/2}|z|} \cdot \begin{bmatrix} \sin^{\frac{1}{2}} w \cos w m_{t,-}(w) & -\sin^{\frac{1}{2}} w \cos w t_-(w) \sin(2\phi) & -\frac{2}{k_o(\epsilon_r - \sin^2 w)^{1/2}} \sin^{\frac{3}{2}} w \cos^2 w t_v(w) \cos \phi \\ -\sin^{\frac{1}{2}} w \cos w t_-(w) \sin(2\phi) & \sin^{\frac{1}{2}} w \cos w m_{t,+}(w) & -\frac{2}{k_o(\epsilon_r - \sin^2 w)^{1/2}} \sin^{\frac{3}{2}} w \cos^2 w t_v(w) \sin \phi \\ -\frac{2}{k_o} \sin^{\frac{3}{2}} w \cos w t_v(w) \cos \phi & -\frac{2}{k_o} \sin^{\frac{3}{2}} w \cos w t_v(w) \sin \phi & \frac{2}{k_o(\epsilon_r - \sin^2 w)^{1/2}} \sin^{\frac{5}{2}} w \cos w t_v(w) \end{bmatrix}; \quad (\text{B-3})$$

where the saddle point is defined as $\cos w_s = (z + z')/r$ for $\bar{\bar{\mathbf{G}}}_r(\cdot)$ and $\cos w_s \approx z/\rho$ for $\bar{\bar{\mathbf{G}}}_t(\cdot)$, and the following ground reflection and transmission coefficient-related expressions are needed:

$$m_{r,\pm}(w) = r_-(w) \pm r_+(w) \cos(2\phi); \quad (\text{B-4})$$

$$m_{t,\pm}(w) = t_+(w) \pm t_-(w) \cos(2\phi); \quad (\text{B-5})$$

$$r_{\pm}(w) = \frac{r_h(w)}{k_o \cos w} \pm \frac{\cos w r_v(w)}{k_o}; \quad (\text{B-6})$$

$$t_{\pm}(w) = \frac{t_h(w)}{k_o (\varepsilon_r - \sin^2 w)^{1/2}} \pm \frac{\cos w t_v(w)}{k_o}; \quad (\text{B-7})$$

$$r_v(w) = \frac{\varepsilon_r \cos w - (\varepsilon_r - \sin^2 w)^{1/2}}{\varepsilon_r \cos w + (\varepsilon_r - \sin^2 w)^{1/2}}; \quad (\text{B-8})$$

$$r_h(w) = \frac{\cos w - (\varepsilon_r - \sin^2 w)^{1/2}}{\cos w + (\varepsilon_r - \sin^2 w)^{1/2}}; \quad (\text{B-9})$$

$$t_{v,h}(w) = 1 + r_{v,h}(w). \quad (\text{B-10})$$

1 DEFENSE TECHNICAL
(PDF) INFORMATION CTR
DTIC OCA

2 DIRECTOR
(PDFS) US ARMY RESEARCH LAB
RDRL CIO LL
IMAL HRA MAIL & RECORDS MGMT

1 GOVT PRINTG OFC
(PDF) A MALHOTRA

3 DIRECTOR
(PDF) US ARMY RESEARCH LAB
RDRL SER U
D LIAO
T DOGARU
A SULLIVAN

2 US ARMY RDECOM CERDEC
(PDF) INTELLIGENCE & INFO WARFARE DIRECTORATE (I2WD)
ATTN RDER IWI TC
JOHN CUA
ADAM MELBER